



Title	Conformational, Dimensional, and Hydrodynamic Properties of Amylose Tris(n-butylcarbamate) in Tetrahydrofuran, Methanol, and Their Mixtures
Author(s)	Terao, Ken; Murashima, Maiko; Sano, Yuichi et al.
Citation	Macromolecules. 2009, 43(2), p. 1061-1068
Version Type	AM
URL	<a href="https://hdl.handle.net/11094/77669">https://hdl.handle.net/11094/77669</a>
rights	Copyright © 2009 American Chemical Society
Note	

*The University of Osaka Institutional Knowledge Archive : OUKA*

<https://ir.library.osaka-u.ac.jp/>

The University of Osaka

# Conformational, Dimensional, and Hydrodynamic Properties of Amylose Tris(*n*-Butylcarbamate) in Tetrahydrofuran, Methanol, and Their Mixtures

*Ken Terao,<sup>\*,†</sup> Maiko Murashima,<sup>†</sup> Yuichi Sano,<sup>†</sup> Shota Arakawa,<sup>†</sup> Shinichi Kitamura,<sup>‡</sup> and Takashi  
Norisuye<sup>†</sup>*

Department of Macromolecular Science, Osaka University, 1-1 Machikaneyama-cho, Toyonaka, Osaka  
560-0043, Japan, Graduate School of Life and Environmental Sciences, Osaka Prefecture University,  
Gakuen-cho, Nakaku, Sakai, Osaka 599-8531, Japan.

Running title: Amylose Tris(*n*-butylcarbamate) in Solution

\* Corresponding author. E-mail: kterao@chem.sci.osaka-u.ac.jp

† Osaka University

‡ Osaka Prefecture University

ABSTRACT: Twelve amylose tris(*n*-butylcarbamate) (ATBC) samples ranging in weight-average molecular weight from  $1.7 \times 10^4$  to  $1.7 \times 10^6$  have been prepared and studied by light and small-angle X-ray scattering, sedimentation equilibrium, viscosity, infrared absorption (IR), and optical rotation in methanol (MeOH), tetrahydrofuran (THF), and their mixtures at 25 °C (or 20 – 25 °C for IR). Data for the mean-square radius of gyration, the particle scattering function, and the intrinsic viscosity are analyzed on the basis of the wormlike chain to yield  $h$  (contour length per residue) = 0.32 nm and  $\lambda^{-1}$  (Kuhn's segment length) = 11 nm in MeOH and  $h = 0.26$  nm and  $\lambda^{-1} = 75$  nm in THF. The high stiffness in THF indicated by  $\lambda^{-1} = 75$  nm is most likely due to the intramolecular hydrogen bonding (between C=O and NH groups of ATBC) observed as the splitting amide I band in the IR spectra. Furthermore, the  $h$  value in this solvent is considerably smaller than the helix pitches per residue of 0.37 – 0.40 nm for amylose triesters in the crystalline state and those of 0.32 – 0.42 nm for semiflexible amylose tris(phenylcarbamate) in various solvents ( $\lambda^{-1} = 15 - 24$  nm), indicating that the ATBC chain forms a tightly wound helix in THF. As the number of intramolecular hydrogen bonds decreases, i.e., as the MeOH content increases in THF-MeOH mixed solvents,  $\lambda^{-1}$  decreases while  $h$  increases. These relationships are successfully explained by a two-state model in which each chain consists of randomly distributed semiflexible (loosely helical) and rodlike (rigid helical) sequences. The resultant  $h$  values for the rodlike and semiflexible portions are 0.25 – 0.26 and 0.32 nm, respectively.

## Introduction

Intramolecular hydrogen bonding (H-bonding) may play a decisive role in the conformation of a polymer chain in solution, in that it often stabilizes the secondary structure of biological and synthetic polymers, *e.g.*,  $\alpha$ -helices of polypeptides,<sup>1</sup> some foldamers,<sup>2,3</sup> and several synthetic helical polymers.<sup>4,5</sup> Amylose tris(carbamate)s, which have three pairs of N-H and C=O groups capable of forming H-bonds on each pyranose ring, can be classified into such polymers.

Several decades ago, Bittiger and Keilich<sup>6</sup> inferred on the basis of circular dichroism (CD) and optical rotatory dispersion curves in 1,4-dioxane (DIOX) that amylose tris(phenylcarbamate) (ATPC) in solution should assume a helical conformation stabilized by the H-bonds between its N-H and C=O groups. Further, Burchard et al. showed the polymer to be quite stiff in a mixed theta solvent<sup>7</sup> and analyzed its dimensional properties in terms of a few models.<sup>8</sup> In recent work, we detected such intramolecular H-bonds in DIOX and 2-ethoxyethanol (2EE) from the split amide I band in infrared absorption (IR) spectra.<sup>9</sup> The helix pitches (or contour lengths) per residue  $h$  ( $= 0.33$  nm) in DIOX and 2EE were slightly shorter than those in esters and a ketone ( $0.37 - 0.42$  nm).<sup>10</sup> This was a measurable difference in  $h$ , but spectroscopic information in the ester and ketone solvents could not be obtained in a relevant range of wavelength. Hence, for the purpose of investigating the relationship between the chain conformation and H-bonding, further solution work with ATPC did not seem so inviting.

Amylose tris(*n*-butylcarbamate) (ATBC, Chart 1), which can be used as a chiral stationary phase in gas chromatography,<sup>11</sup> should be suitable for this purpose because of its good solubility in methanol (MeOH) and tetrahydrofuran (THF) allowing infrared absorption measurements around the amide I band. This band sensitively reflects the H-bonding of C=O groups not only of ATPC but also of amylose tris(3,5-dimethylphenylcarbamate) (ADMPC).<sup>12</sup> In this work, we studied conformational, dimensional, and hydrodynamic properties of ATBC in THF, MeOH, and their mixtures by light and small-angle X-ray scattering, viscosity, IR, and optical rotation, and found that the polymer assumes a rigid, tight, helical conformation in THF and a relatively flexible, more extended helical conformation in MeOH. When expressed in terms of Kuhn's segment length of the wormlike chain<sup>13</sup> (or more

generally the stiffness parameter in the helical wormlike chain<sup>14,15,16</sup>), the rigidity of the ATBC helix in the former solvent was as high as 75 nm and that in the latter solvent was 11 nm. Analyses of the measured properties leading to these findings are described below, along with the conformation change in THF-MeOH mixtures. It should be noted that few studies have been reported on conformational properties of amylose tris(carbamate)s other than ATPC and ADMPC.<sup>17,18,19</sup>

## Experimental Section

**Preparation of ATBC Samples.** ATBC samples were synthesized from amylose (eight enzymatically synthesized samples<sup>20</sup>) and an excess amount of *n*-butylisocyanate in a manner similar to that reported previously for the preparation of ATPC;<sup>9</sup> our method was also substantially the same as that employed by Kubota et al. for amylose tris (cyclohexyl carbamate).<sup>21</sup> The amylose samples ranged in weight-average molecular weight  $M_w$  from  $6 \times 10^3$  to  $1 \times 10^6$  and had polydispersity indices PDI (ratios of  $M_w$  to the number-average molecular weight  $M_n$ ) less than 1.2. A typical procedure for the ATBC synthesis was as follows.

Pyridine (60 cm<sup>3</sup>) and *n*-butylisocyanate (19 g) were added to an amylose (3.5 g) solution of *N,N'*-dimethylacetoamide (33 cm<sup>3</sup>, containing 3.0 g LiCl), and the reaction mixture was stirred at 80 °C for 24 hours. The solution was then poured into a large amount of water to precipitate ATBC. The product was further purified by successive fractional precipitation with MeOH as a solvent and water as a precipitant to remove LiCl, unreacted *n*-butylisocyanate, and by-products. *N,N'*-dimethylacetoamide (dehydrated grade), LiCl, *n*-butylisocyanate, and MeOH (for the fractionation) were used without further purification, while pyridine was purified by fractional distillation over CaH<sub>2</sub>.

Twelve appropriate middle fractions were chosen for the present work. They were reprecipitated from MeOH solutions into water and dried in vacuum at 80 °C for 3 days. The degree of substitution (DS) determined from the mass ratio of carbon to nitrogen by elemental analysis for each sample is presented in Table 1. Its values close to 3 ( $\pm 0.4$ ) indicate that the three hydroxyl groups on each glucose unit of amylose were fully substituted to *n*-butylcarbamate for any sample. The chemical

structure was confirmed by observed chemical shifts of 0.8 – 1 ppm (methyl protons), 1.2 – 1.6 ppm (methylene protons), 2.8 – 5.4 ppm (methylene and pyranose protons), and 6 – 7.4 ppm (NH protons) in  $^1\text{H}$  NMR spectra (JEOL GSX-400) for samples ATBC17K and ATBC130K in  $\text{CDCl}_3$  at 30 °C and also by absorption bands (in wavenumber) of  $3320\text{ cm}^{-1}$  for NH stretching and  $1705\text{ cm}^{-1}$  for C=O stretching in IR spectra (JASCO FT/IR8300, the KBr method) for ATBC130K, ATBC260K, ATBC460K, and ATBC900K. The PDI value for each sample was determined by size-exclusion chromatography combined with right and low-angle light scattering and refractive index detectors (SEC-LS), with the result listed in the third column in Table 1.

**Light and Small-Angle X-ray Scattering.** Static light scattering (SLS) measurements were made on a Fica-50 light scattering photometer with vertically polarized incident light of 436-nm wavelength for ATBC1700K, ATBC900K, ATBC700K, ATBC460K, ATBC250K, and ATBC53K in MeOH, for ATBC900K, ATBC700K, ATBC490K, ATBC460K, ATBC260K, and ATBC250K in THF, and for ATBC900K, ATBC700K, and ATBC250K in a THF-MeOH mixture of  $\phi_m$  (the volume fraction of MeOH) = 0.5, all at 25 °C (see ref 9 for the experimental details). The specific refractive index increments  $\partial n/\partial c$  for ATBC55K and ATBC17K in MeOH and ATBC900K in THF at 25 °C were determined using a Schulz-Cantow type differential refractometer. The  $\partial n/\partial c$  values in MeOH were 0.151, 0.147, and  $0.145\text{ cm}^3\text{g}^{-1}$  at  $\lambda_0$  (the wavelength) = 436, 546, and 633 nm, respectively, while those in THF were 0.0830, 0.0799,  $0.0795\text{ cm}^3\text{g}^{-1}$  at 436, 546, and 633 nm, respectively. No substantial difference in  $\partial n/\partial c$  between ATBC55K and ATBC17K was observed for MeOH solutions. The THF and MeOH used were fractionally distilled over  $\text{CaH}_2$ .

Small-angle X-ray scattering (SAXS) experiments were carried out for ATBC55K and ATBC17K in THF-MeOH mixtures with  $\phi_m$ 's of 0.25, 0.5, 0.75, and 1 using a Rigaku R-Axis IV++ or a Rigaku R-Axis VII imaging plate detector at the BL40B2 beamline in SPring-8. At  $\phi_m = 0$ , i.e., in pure THF, samples ATBC53K and ATBC17K were studied. The camera length and  $\lambda_0$  were set to be 1500 mm and 0.1 nm, respectively.

The intensity data obtained from SLS and SAXS were analyzed by use of the square-root plot.<sup>22</sup> The particle scattering function  $P(k)$  was evaluated as the ratio of the scattering intensity at zero angle to that at scattering angle  $\theta$  at infinite dilution, where  $k$  denotes the magnitude of the scattering vector.

**Sedimentation Equilibrium.** Sedimentation equilibrium measurements were made on ATBC17K, ATBC55K, ATBC110K, and ATBC130K in MeOH at 25 °C using a Beckman Optima XL-I analytical ultracentrifuge. Test solutions and the solvent were injected in 12-mm double sector cells and spun at 6,500 – 20,000 rpm. Detailed experimental procedures and data analysis including evaluation of the  $z$ -average molecular weight  $M_z$  were described in ref 23. The partial specific volume was determined to be 0.833 and 0.820 cm<sup>3</sup>g<sup>-1</sup> for ATBC17K and ATBC55K, respectively, in MeOH at 25 °C using an Anton Paar DMA5000 densitometer. The  $\partial n/\partial c$  at  $\lambda_0 = 675$  nm was estimated from the above-mentioned data with the aid of  $\partial n/\partial c$  vs  $\lambda_0^{-2}$  plot.

**Viscometry.** The intrinsic viscosity  $[\eta]$  at zero shear rate and the Huggins constant  $k'$  in THF-MeOH mixtures with different  $\phi_m$  at 25 °C were determined using conventional capillary viscometers and/or a four-bulb low-shear capillary viscometer of the Ubbelohde type. For low molecular weight samples, the relative viscosity was evaluated by taking into account the difference between the solution and solvent densities.

**Optical Rotation.** Specific optical rotations  $[\alpha]_{280}$  at  $\lambda_0 = 280$  nm were determined for ATBC900K, ATBC460K, and ATBC55K in THF-MeOH mixtures at 25°C using a JASCO J720WO spectropolarimeter (with an optical rotatory dispersion detector) and a quartz cell of 10 cm path length. The polymer mass concentration  $c$  was adjusted to  $1 - 2 \times 10^{-2}$  g cm<sup>-3</sup>.

**Infrared Absorption and DFT calculations.** Fourier transform infrared absorption (FT-IR) measurements were made for ATBC solutions and the solvents at room temperature (20 – 25 °C) and at  $c \sim 1 \times 10^{-2}$  g cm<sup>-3</sup> on an Excalibur FTS-300 FT-IR spectrometer (Bio-Rad Labs.) with a solution cell made of CaF<sub>2</sub> and having 0.05 mm path length.

To assign amide I peaks in experimental IR spectra, calculations based on the density functional theory (DFT) were performed using the Gaussian 03 program.<sup>24</sup> Methyl methylcarbamate (MMC) was chosen as a model compound for the carbonyl groups of ATBC. The absorption wavenumbers  $\nu$  of amide I and II bands of MMC were found to be 1728 and 1521  $\text{cm}^{-1}$ , respectively, when its conformation was optimized using the B3LYP/6-311+G(d,p) level theory with a scaling factor of 0.9679.<sup>25</sup> The absorption bands for an H-bonding carbonyl group were calculated in the following manner. First, an OH group of MeOH or an NH group of an MMC molecule was placed near by the C=O group of another MMC molecule with an appropriate direction. Then the conformation of the complex was optimized by the above-mentioned DFT method. The resultant  $\nu$  values (amide I) perturbed by MeOH and MMC were obtained as 1704  $\text{cm}^{-1}$  and 1702  $\text{cm}^{-1}$ , respectively.

## Results and Discussion

**Molecular Weight and Second Virial Coefficient.** Figure 1 shows sedimentation equilibrium data for ATBC samples in MeOH (panel a) and SLS data in MeOH (panel b) and in THF (panel c), all at 25 °C. Here,  $M_{\text{app}}$  is the apparent molecular weight,  $\bar{c}$  is the mean concentration defined by  $(c_a + c_b)/2$ , with  $c_a$  and  $c_b$  being the polymer mass concentrations at the liquid meniscus and cell bottom, respectively,  $K$  is the optical constant, and  $R_0$  is the zero-angle value of the excess reduced scattering intensity  $R_\theta$  (at scattering angle  $\theta$ ). The values of  $M_w$  and  $A_2$  (the second virial coefficient) evaluated from the intercepts and slopes of the indicated straight lines are summarized in Table 1, along with those of  $M_z/M_w$  from sedimentation equilibrium. The  $M_w$  values in MeOH and THF (for ATBC900K, ATBC700K, ATBC460K, and ATBC250K) agree with each other within experimental errors ( $\pm 4$  %). The  $A_2$  values ranging from 0.7 to  $4 \times 10^{-4} \text{ cm}^3 \text{ mol g}^{-2}$  in the two solvents indicate that both are good solvents for ATBC. While  $A_2$  (and  $M_w$ ) in the mixed solvent was not determined owing to the difficulty to obtain its refractive index increments  $(\partial n/\partial c)_\mu$  at fixed chemical potentials  $\mu$  of diffusible components, THF-MeOH mixtures should also be good solvents because no turbidity were found in the range of temperature between 0 and 40 °C.

Figure 2 illustrates the angular dependence of  $P(k)^{-1/2}$  for the indicated ATBC samples in MeOH and THF. The  $z$ -average mean-square radii of gyration  $\langle S^2 \rangle_z$  determined from the initial slopes (the dashed lines) of the curves are presented in Table 1, in which  $[\eta]$  data are also presented.

**Dimensional and Hydrodynamic Properties.** *Molecular weight dependence of  $\langle S^2 \rangle_z$  and  $[\eta]$ .*

Figure 3 illustrates the molecular weight dependence of  $\langle S^2 \rangle_z^{1/2}$  for ATBC in THF and MeOH at 25 °C. The data points in either solvent are fitted by a curve convex upward, whose slope decreases with increasing  $M_w$  from 0.9 to 0.7 and 0.7 to 0.55 in THF and MeOH, respectively, indicating that the ATBC chain is significantly stiffer in the former solvent than in the latter. The figure includes the  $\langle S^2 \rangle_z^{1/2}$  data in the THF-MeOH mixture of  $\phi_m = 0.5$ . The curve fitting the triangles suggests that the polymer in this mixture has a stiffness intermediate between those in THF and MeOH.

The intrinsic viscosities in THF, MeOH, and their mixtures of  $\phi_m = 0.25, 0.50$ , and  $0.75$  are plotted double-logarithmically against  $M_w$  in Figure 4. The viscosity exponent is 1.2 around  $M_w = 10^5$  in THF and decreases with increasing  $\phi_m$  to 0.85 in MeOH, being consistent with the higher stiffness of the ATBC chain in the former solvent found above from  $\langle S^2 \rangle_z$ .

*Analysis of  $\langle S^2 \rangle_z$ .* We analyze the present  $\langle S^2 \rangle_z$  data in terms of the wormlike chain with or without excluded volume using the expression<sup>26</sup>

$$\langle S^2 \rangle_0 = \frac{L}{6\lambda} - \frac{1}{4\lambda^2} + \frac{1}{4\lambda^3 L} - \frac{1}{8\lambda^4 L^2} [1 - \exp(-2\lambda L)] \quad (1)$$

for the unperturbed mean-square radius of gyration  $\langle S^2 \rangle_0$  and the Domb-Barrett<sup>27</sup> equation for the expansion factors  $\alpha_s^2 (= \langle S^2 \rangle / \langle S^2 \rangle_0)$  in the quasi-two-parameter (QTP) theory.<sup>14,28,29</sup> Here,  $\lambda^{-1}$  is the Kuhn segment length and  $L$  is the contour length equal to the ratio of  $M$  (the molar mass) to  $M_L$  (the molar mass per unit contour length). In the QTP scheme,  $\langle S^2 \rangle$  is a function of  $M/M_L$ ,  $\lambda^{-1}$ , and  $B$  (the excluded-volume strength). The three unknowns ( $M_L$ ,  $\lambda^{-1}$ , and  $B$ ) were determined by curve fitting, with the result summarized in Table 2; the values of  $B$  in THF and in the mixture of  $\phi_m = 0.5$  need not

be estimated because excluded-volume effects were negligible in the range of  $M_w$  studied. The solid lines fitting the data points in Figure 3 represent the theoretical values, while the dashed line (drawn for MeOH solutions) refers to the unperturbed state. The deviation of the solid line for MeOH from the dashed one is only about 6 % at the highest  $M_w$ , showing that the intramolecular excluded-volume effect in the solvent is insignificant in the molecular weight range studied.

*Analysis of  $P(k)$ .* The Holtzer plots<sup>30</sup> of  $k P(k)$  vs  $k$  for ATBC53K and ATBC17K in THF are shown in Figure 5, along with those for ATBC55K and ATBC17K in MeOH and THF-MeOH mixtures. The data points in THF are quantitatively reproduced by the solid lines computed from Nakamura and Norisuye's theory<sup>31</sup> for wormlike cylinders with  $M_L = 1780 \text{ nm}^{-1}$ ,  $\lambda^{-1} = 78 \text{ nm}$  (the value from  $\langle S^2 \rangle_z$ ), and  $d = 1.1 \text{ nm}$ . These lines are almost indistinguishable from the dashed curves (mostly hidden behind the solid lines) calculated for the straight cylinders<sup>31,32</sup> with  $M_L = 1780 \text{ nm}^{-1}$  and the diameter  $d = 1.1 \text{ nm}$ . Thus, the scattering functions of the low  $M_w$  samples do not allow  $\lambda^{-1}$  to be estimated.

In MeOH, a broad but clear peak is observed for ATBC55K (Figure 5), indicating a lower chain stiffness in the solvent than in THF. By curve fitting,  $M_L$ ,  $\lambda^{-1}$ , and  $d$  in this solvent have been estimated on the basis of the theory<sup>31</sup> for unperturbed wormlike cylinders to be  $1450 \pm 30 \text{ nm}^{-1}$ ,  $9 \pm 2 \text{ nm}$ , and  $1.1 \pm 0.1 \text{ nm}$ , respectively. The theoretical solid curves calculated for ATBC55K and ATBC17K with these parameters are appreciably higher than the dashed curves drawn for  $\lambda^{-1} = \infty$ , thus showing unequivocal determination of  $\lambda^{-1}$  in MeOH. In the mixtures of  $\phi_m = 0.25, 0.5$ , and  $0.75$ , the  $P(k)$  data were similarly analyzed; at  $\phi_m = 0.5$  and  $0.25$ , the  $\lambda^{-1}$  values from  $\langle S^2 \rangle_z$  and  $[\eta]$  (see below), respectively, were assumed. The model parameters obtained from  $P(k)$  are presented in Table 2. It should be noted in relation to the  $d$  values that the chain thickness contribution<sup>33</sup>  $d^2/8$  to  $\langle S^2 \rangle$  of a wormlike cylinder is at most 2% and hence negligible in the  $M_w$  range studied.

*Analysis of  $[\eta]$ .* If the Yamakawa-Fujii-Yoshizaki viscosity theory<sup>14,34,35</sup> for unperturbed wormlike cylinders is combined with the Barrett equation<sup>36</sup> for the viscosity expansion factor in the QTP scheme,<sup>14</sup>  $[\eta]$  for a given  $M$  is determined by the four parameters,  $M_L$ ,  $\lambda^{-1}$ ,  $d$ , and  $B$ . In our curve-fitting

procedure, the last parameter was considered only in pure MeOH, but  $M_L$  in it was taken to be  $1440 \text{ nm}^{-1}$ , the mean from  $\langle S^2 \rangle_z$  and  $P(k)$ ; furthermore, at  $\phi_m = 0.25$  and  $0.75$ , the values from  $P(k)$  were assumed. The estimated parameters are summarized in Table 2, and the theoretical curves are shown in Figure 4. The dashed line again refers to the unperturbed state.

In Table 2, the values of  $M_L$  and  $\lambda^{-1}$  from  $[\eta]$  are seen to be in substantial agreement with those from  $\langle S^2 \rangle_z$  and  $P(k)$ , demonstrating that the wormlike chain allows a consistent description of the measured dimensional and hydrodynamic properties of ATBC. The  $d$  values from  $[\eta]$  are, however, 2 – 3 times larger than those from  $P(k)$ . This is probably because the latter reflects the electron density profile around the chain contour.<sup>14</sup> Similar behavior was also reported for ATPC<sup>9,10</sup> and other polymers<sup>37,38</sup> in dilute solution.

**Wormlike Chain Parameters.** Table 3 presents the value of  $\lambda^{-1}$  (the mean from the three different properties) and the contour length per residue  $h$  ( $= M_0/M_L$ ) as a function of  $\phi_m$ , where  $M_0$  denotes the molar mass of the repeating unit of ATBC. As  $\phi_m$  decreases,  $h$  slightly decreases, while  $\lambda^{-1}$  increases significantly and reaches a value as high as  $75 \text{ nm}$  in THF. No such high stiffness has ever been reported for other carbamate derivatives of polysaccharides including cellulose,<sup>39,40,41</sup> chitosan,<sup>42</sup> and mannan.<sup>43</sup> It is interesting to note that amylose has a much smaller  $\lambda^{-1}$  of  $4 \text{ nm}$  in various solvents<sup>44,45</sup> and a relatively large value of  $18 \text{ nm}$  in a metal complex solvent.<sup>46</sup> The high rigidity of the ATBC chain in THF is supported by our finding<sup>47</sup> that a concentrated THF solution of the polymer ( $c = 0.35 \text{ g cm}^{-3}$ ) shows liquid crystallinity. On the other hand, the  $h$  value  $0.26 \text{ nm}$  in THF, measurably smaller than  $0.32 \text{ nm}$  in MeOH and  $0.33 \text{ nm}$  for locally helical ATPC in DIOX and 2EE,<sup>9</sup> is much smaller than those of  $0.37 - 0.42 \text{ nm}$  for ATPC in ester and ketone solvents<sup>10</sup> and the helix pitches per residue ( $0.37 - 0.40 \text{ nm}$ ) of amylose triesters in the crystalline state.<sup>48,49</sup> Hence, ATBC in THF may be considered to have a rigid, tight, helical structure; note that the helical wormlike chain model is not necessary for use in analyzing our solution data because the centroid of a helical, stiff polymer chain is represented by the wormlike chain.<sup>50</sup>

**Infrared Absorption and Optical Rotation.** If a certain local conformation change causes the observed decrease in  $h$  and increase in  $\lambda^{-1}$  with a decrease in  $\phi_m$ , it should be detected as changes in IR spectrum and/or optical rotation. Figure 6 displays IR spectra for ATBC460K in THF, MeOH, and their mixtures. While the peaks observed between 1100 and 1600  $\text{cm}^{-1}$  are essentially independent of  $\phi_m$ , the absorption band around 1700 – 1740  $\text{cm}^{-1}$  significantly varies with  $\phi_m$ . The double peak observed in THF is fitted by two Gaussian distributions centered at 1737 and 1698  $\text{cm}^{-1}$ . These are fairly close to the theoretical values of 1728 and 1702  $\text{cm}^{-1}$  for free and H-bonding carbonyl groups of MMC, respectively (see Experimental Section). On the other hand, the observed single peak in MeOH follows the normal distribution with the mean value of 1718  $\text{cm}^{-1}$ , which is larger than the theoretical value 1704  $\text{cm}^{-1}$ . This discrepancy and the broad distribution are most likely due to the high mobility of the H-bonding solvent molecules.

IR spectra at the amide I band in THF-MeOH mixtures were successfully separated into the aforementioned three components, as indicated by thin lines in Figure 6. Since the total areas of this band at the five  $\phi_m$ 's are substantially the same, we regard the absorption coefficients for the three peaks as equal and denote the area fractions (i.e., the number fractions of the respective components) as  $f_{1737}$ ,  $f_{1718}$ , and  $f_{1698}$  at 1737, 1718, and 1698  $\text{cm}^{-1}$ , respectively. Both  $f_{1737}$  and  $f_{1698}$  decrease (and hence  $f_{1718}$  increases) with an increase in  $\phi_m$ , and the more abrupt diminution of the former than the latter suggests that the free C=O has higher tendency to form H-bonds with MeOH than does the H-bonding C=O.

Figure 7 illustrates the  $\phi_m$ -dependence of  $f_{1698}$  and  $-[\alpha]_{280}$ . The curves of  $f_{1698}$  and  $-[\alpha]_{280}$  almost overlap each other, indicating that  $f_{1698}$  reflects a local-conformational property such as the helix content. The figure also shows that  $f_{1698}$  and  $[\alpha]_{280}$  are independent of  $M_w$  and undergo monotonic and gradual solvent-dependence. Thus, the cooperativity of the helical conformation is much less important for ATBC than for  $\alpha$ -helical polypeptides<sup>51,52</sup> or even negligible. In other words, intramolecular H-

bonds randomly break as  $\phi_m$  increases, and thus the ATBC chain consists of alternating rigid (helical) and semiflexible (looser helical) portions with and without intramolecular H-bonding, respectively.

**Solvent-Dependence of Main Chain Conformation.** On the basis of the above considerations, we model the ATBC chain in a given THF-MeOH mixture by a copolymer consisting of R and F monomeric units and denote the Kuhn lengths of the pure R and F chains as  $\lambda_R^{-1}$  and  $\lambda_F^{-1}$ , respectively, and the contour lengths per residue as  $h_R$  and  $h_F$ . We assume the distribution of these units to be completely random. Then  $h$  ( $= M_0L/M$ ) and  $\lambda^{-1}$  leading to eq 1 are given by<sup>53</sup>

$$h = F_R h_R + (1 - F_R) h_F \quad (2)$$

$$\lambda h = F_R \lambda_R h_R + (1 - F_R) \lambda_F h_F \quad (3)$$

where the number fraction  $F_R$  of the R monomer is related to  $f_{1698}$  by

$$F_R = \frac{f_{1698}}{f_R} \quad (4)$$

with  $f_R$  the value of  $f_{1698}$  for the homopolymer R; note that  $f_F$  ( $f_{1698}$  for the F homopolymer) = 0 because  $f_{1698}$  vanishes in MeOH. Elimination of  $F_R$  from eqs 2 and 3 yields

$$h^{-1} - h_F^{-1} = -\frac{h_R^{-1} - h_F^{-1}}{\lambda_F - \lambda_R} (\lambda - \lambda_F) \quad (5)$$

which predicts that  $h^{-1}$  varies linearly with  $\lambda$ .

Panel a of Figure 8 shows the plot of  $h^{-1}$  vs  $\lambda$  constructed for ATBC in THF-MeOH mixtures according to eq 5, while panel b presents those of  $h$  and  $\lambda h$  against  $f_{1698}$  based on eqs 2 and 3, respectively. These plots are linear, implying that the two-state model assumed is suitable for

describing the conformation change of ATBC in the mixed solvent system. The intercepts of the straight lines in panel b give  $h_F = 0.32$  nm and  $\lambda_F^{-1} = 11$  nm (see also Table 3). With these values for the F polymer, we obtain the relation  $h_R^{-1} = 4.0 - 9.8\lambda_R$  (nm<sup>-1</sup>) for the R polymer using eq 5 and the slope (-9.8) of the line in panel a. Although any single relation does not allow determination of two unknowns, we can estimate  $h_R$  to be in a narrow range between 0.25 and 0.26 nm on the basis of the possible  $\lambda_R$  range ( $0 < \lambda_R < 1/75$  nm<sup>-1</sup>); note that the contribution of  $-9.8\lambda_R$  in the above relation to  $h_R$  is at most 3.3 %. The  $h_R$  of 2.5 – 2.6 nm does not differ from the directly estimated value of 0.26 nm in THF, both being much shorter than 0.37 – 0.42 nm for ATPC in ester and ketone solvents<sup>8</sup> and for amylose triesters in the crystalline state.<sup>48,49</sup> Using the  $h$  vs  $f_{1698}$  relation (the upper straight line in panel b) with  $h_R = 0.25 - 0.26$  nm, we estimate  $f_R$  ( $> f_{1698}$  in THF) to be 0.52 – 0.58. The  $f_R$  in this range is fairly close to the value 2/3 corresponding to the case in which two C=O groups per repeating unit of the R chain form H-bonds (*i.e.*,  $f_R = 2/3$ ).

We add that the copolymer nature mentioned above does not impair the wormlike chain behavior of  $[\eta]$  and  $P(k)$  if the diameters of the R and F chains are not very different. In fact, the wormlike chain parameters ( $M_L$  and  $\lambda^{-1}$ ) determined from the different methods are in excellent agreement with one another for ATBC in the mixed solvent of  $\phi_m = 0.5$  and for an actual copolymer.<sup>53</sup> This is also supported by the theoretical fact that the conformational defect in the broken wormlike chain model has no significant effect on dimensional and hydrodynamic properties.<sup>54</sup>

**Possible Helical Structure.** To determine the helical structure of an amylosic chain, at least two torsion angles should be given even when the glucosidic bond angle and the conformation of the pyranose ring are fixed, but we have only one piece of information, that is,  $h$ . We note that the 2D NOESY NMR method reported to estimate the distance between two hydrogen atoms on consecutive pyranose rings of ADMPC<sup>17</sup> is not applicable to our system since the signal of some methylene protons of ATBC is hardly distinguishable from that of some pyranose protons. Therefore, we can deduce the helical structure of ATBC on condition that the helical symmetry is available.

We chose a six-fold left-handed helix of  $h = 0.25$  nm, and attempted to construct the structure of a 14-mer ATBC molecule using the sugar builder of the Hyperchem version 8 software. An MM2 minimization was performed on the molecule using the ChemBioOffice Ultra 11.0 (some parameters were guessed by the algorithm of the software) after the molecular dynamics simulation with the same force field for 20 ps (10000 steps) at 300K. In these procedures, oxygen atoms between every two consecutive pyranose rings were fixed to keep the  $h$  value. The resultant 3D structure displayed in Figure 9 shows that most of the C=O groups at C2 and C6 of the respective pyranose rings form H-bonds with the NH groups at C3 and C6 on the next adjoining pyranose rings, respectively (the white dotted segments), whereas each C=O at C3 has no or a weak H-bond with the NH group on the same repeat unit. Namely, the number fraction of strongly H-bonding C=O groups is roughly 0.6, a value fairly close to experimentally estimated  $f_R$  of 0.52 – 0.58. The agreement suggests that the displayed 3D conformation is one of the possible helical structures for ATBC in THF. We note, however, that this discussion also applies to five or seven fold helices. It is thus intriguing to determine the crystal structure of the amylose derivative, but we wish to leave the determination for future work.

## Conclusions

ATBC in THF assumes a rigid helical conformation with  $\lambda^{-1} = 75$  nm and  $h = 0.26$  nm stabilized by intramolecular H-bonds. This helix pitch per residue is much shorter than the reported values for ATPC in ketone and ester solvents (0.37 – 0.42 nm)<sup>10</sup> and for amylose triesters in the crystalline state (0.37 – 0.40 nm).<sup>48,49</sup> On the other hand, the ATBC helix in MeOH is much more flexible ( $\lambda^{-1} = 11$  nm) and slightly extended ( $h = 0.32$  nm), as is the case for the ATPC helices in DIOX and 2EE.<sup>7</sup> In mixtures of THF and MeOH,  $\lambda^{-1}$ ,  $h$ , the number fraction  $f_{1698}$  of the intramolecular H-bonding, and  $[\alpha]_{280}$  change monotonically with MeOH content. The last two quantities, independent of  $M_w$ , indicate that the cooperativity does not play an important role in the solvent-induced conformation change for the polymer – mixed solvent system. This conformation change is successfully explained by a two-state

model consisting of random sequences of rodlike and semiflexible portions, i.e., by random breaking of intramolecular hydrogen bonds in ATBC accompanying an increase in MeOH content.

**Acknowledgment.** We are indebted to Prof. Takahiro Sato (Osaka Univ.) for valuable discussions and comments, Prof. Tadashi Inoue (Osaka Univ.) for allowing us to use the FT-IR instrument, and Mr. Masahiro Ohtoh (Osaka Univ.) for synthesis of an ATBC sample. The synchrotron radiation experiments were performed at the BL40B2 in SPring-8 with the approval of the Japan Synchrotron Radiation Research Institute (JASRI) (Proposal #2007A1034 and #2007B1296).

---

## References and Notes

1. Alberts, B.; Johnson, A.; Lewis, J.; Raff, M.; Roberts, K.; Walter, P. *Molecular Biology of the Cell*, 4th ed.; Garland Science: New York, 2002.
2. Gellman, S. H. *Acc. Chem. Res.* **1998**, *31*, 173-180.
3. Hill, D. J.; Mio, M. J.; Prince, R. B.; Hughes, T. S.; Moore, J. S. *Chem. Rev.* **2001**, *101*, 3893-4011.
4. Okoshi, K.; Sakurai, S.-I.; Ohsawa, S.; Kumaki, J.; Yashima, E. *Angew. Chem. Int. Ed.* **2006**, *45*, 8173-8176.
5. Terada, K.; Masuda, T.; Sanda, F. *Macromolecules* **2009**, *42*, 913-920.
6. Bittiger, H.; Keilich, G. *Biopolymers* **1969**, *7*, 539-556.
7. Burchard, W. *Br. Polym. J.* **1971**, *3*, 214-221.
8. Hsu, B.; McWherter, C. A.; Brant, D. A.; Burchard, W. *Macromolecules* **1982**, *15*, 1350-1357.
9. Terao, K.; Fujii, T.; Tsuda, M.; Kitamura, S.; Norisuye, T. *Polym. J.* **2009**, *41*, 201-207.
10. Fujii, T.; Terao, K.; Tsuda, M.; Kitamura, S.; Norisuye, T. *Biopolymers*, **2009**, *91*, 729-736.
11. Schurig, V.; Zhu, J.; Muschalek, V. *Chromatographia* **1993**, *35*, 237-240.
12. Kasat, R. B.; Zvinevich, Y.; Hillhouse, H. W.; Thomson, K. T.; Wang, N.-H. L.; Franes, E. I. *J. Phys. Chem. B.* **2006**, *110*, 14114-14122.

- 
13. Kratky, O.; Porod, G. *Recl. Trav. Chim. Pays-Bas* **1949**, *68*, 1106-1122.
  14. Yamakawa, H. *Helical Wormlike Chains in Polymer Solutions*; Springer: Berlin, 1997.
  15. Yamakawa, H.; Fujii, M. *J. Chem. Phys.* **1976**, *64*, 5222-5228.
  16. Yamakawa, H. *Polym. J.* **1999**, *31*, 109-119.
  17. Yamamoto, C.; Yashima, E.; Okamoto, Y. *J. Am. Chem. Soc.* **2002**, *124*, 12583-12589.
  18. Wenslow, R. M. Jr.; Wang, T. *Anal. Chem.* **2001**, *73*, 4190-4195.
  19. Ma, S.; Shen, S.; Lee, H.; Yee, N.; Senanayake, C.; Nafie, L. A.; Grinberg, N. *Tetrahedron: Asymmetry* **2008**, *19*, 2111-2114.
  20. Kitamura, S.; Yunokawa, H.; Mitsuie, S.; Kuge, T. *Polym. J.* **1982**, *14*, 93-99.
  21. Kubota, T.; Yamamoto, C.; Okamoto, Y. *J. Am. Chem. Soc.* **2000**, *122*, 4056-4059.
  22. Berry, G. C. *J. Chem. Phys.* **1966**, *44*, 4550-4564.
  23. Norisuye, T.; Yanaki, T.; Fujita, H. *J. Polym. Sci. Polym. Phys. Ed.* **1980**, *18*, 547-558.
  24. Frisch, M. J.; Trucks, G. W.; Schlegel, H. B.; Scuseria, G. E.; Robb, M. A.; Cheeseman, J. R.; Montgomery, Jr., J. A.; Vreven, T.; Kudin, K. N.; Burant, J. C.; Millam, J. M.; Iyengar, S. S.; Tomasi, J.; Barone, V.; Mennucci, B.; Cossi, M.; Scalmani, G.; Rega, N.; Petersson, G. A.; Nakatsuji, H.; Hada, M.; Ehara, M.; Toyota, K.; Fukuda, R.; Hasegawa, J.; Ishida, M.; Nakajima, T.; Honda, Y.; Kitao, O.; Nakai, H.; Klene, M.; Li, X.; Knox, J. E.; Hratchian, H. P.; Cross, J. B.; Bakken, V.; Adamo, C.; Jaramillo, J.; Gomperts, R.; Stratmann, R. E.; Yazyev, O.; Austin, A. J.; Cammi, R.; Pomelli, C.; Ochterski, J. W.; Ayala, P. Y.; Morokuma, K.; Voth, G. A.; Salvador, P.; Dannenberg, J. J.; Zakrzewski, V. G.; Dapprich, S.; Daniels, A. D.; Strain, M. C.; Farkas, O.; Malick, D. K.; Rabuck, A. D.; Raghavachari, K.; Foresman, J. B.; Ortiz, J. V.; Cui, Q.; Baboul, A. G.; Clifford, S.; Cioslowski, J.; Stefanov, B. B.; Liu, G.; Liashenko, A.; Piskorz, P.; Komaromi, I.; Martin, R. L.; Fox, D. J.; Keith, T.; Al-Laham, M. A.; Peng, C. Y.; Nanayakkara, A.; Challacombe, M.; Gill, P. M. W.; Johnson, B.; Chen, W.; Wong, M. W.; Gonzalez, C.; Pople, J. A. *Gaussian 03, Rev. E.01*; Gaussian, Inc., Wallingford, CT, **2004**.

- 
25. Andersson, M. P.; Uvdal, P. *J. Phys. Chem. A*. **2005**, *109*, 2937-2941.
  26. Benoit, H.; Doty, P. *J. Phys. Chem.* **1953**, *57*, 958-963.
  27. Domb, C.; Barrett, A. J. *Polymer* **1976**, *17*, 179-184.
  28. Yamakawa, H.; Stockmayer, W. H. *J. Chem. Phys.* **1972**, *57*, 2843-2854.
  29. Shimada, J.; Yamakawa, H. *J. Chem. Phys.* **1986**, *85*, 591-599.
  30. Holtzer, A. *J. Polym. Sci.* **1955**, *17*, 432-434.
  31. Nakamura, Y.; Norisuye, T. *J. Polym. Sci., Part B: Polym. Phys.* **2004**, *42*, 1398-1407.
  32. Pedersen, J. S.; Schurtenberger, P. *J. Appl. Crystallogr.* **1996**, *29*, 646-661.
  33. Konishi, T.; Yoshizaki, T.; Saito, T.; Einaga, Y.; Yamakawa, H. *Macromolecules* **1990**, *23*, 290-297.
  34. Yamakawa, H.; Fujii, M. *Macromolecules* **1974**, *7*, 128-135.
  35. Yamakawa, H.; Yoshizaki, T. *Macromolecules* **1980**, *13*, 633-643.
  36. Barrett, A. J. *Macromolecules* **1984**, *17*, 1566-1572.
  37. Hickl, P.; Ballauff, M.; Scherf, U.; Mullen, K.; Lindner, P. *Macromolecules* **1997**, *30*, 273-279.
  38. Terao, K.; Mizuno, K.; Murashima, M.; Kita, Y.; Hongo, C.; Okuyama, K.; Norisuye, T.; Bächinger, H. P.; *Macromolecules* **2008**, *41*, 7203-7210.
  39. Tsuboi, A.; Norisuye, T.; Teramoto, A. *Macromolecules* **1996**, *29*, 3597-3602.
  40. Kasabo, F.; Kanematsu, T.; Nakagawa, T.; Sato, T.; Teramoto, A. *Macromolecules* **2000**, *33*, 2748-2756.
  41. Yanagisawa, M.; Isogai, A. *Biomacromolecules* **2005**, *6*, 1258-1265.
  42. Kuse, Y.; Asahina, D.; Nishio, Y. *Biomacromolecules* **2009**, *10*, 166-173.
  43. Sutter, W.; Burchard W. *Makromol. Chem.* **1978**, *179*, 1961-1980.
  44. Nakanishi, Y.; Norisuye, T.; Teramoto, A.; Kitamura, S. *Macromolecules* **1993**, *26*, 4220-4225.
  45. Norisuye, T. *Polym. J.* **1994**, *26*, 1303-1307.
  46. Seger, B.; Aberle, T.; Burchard, W. *Carbohydr. Polym.* **1996**, *31*, 105-112.

---

47. Significant birefringence was observed at room temperature for an ATBC900K-THF solution ( $c = 0.35 \text{ g cm}^{-3}$ ) when two polarizers were set into the cross-Nicol position. This liquid crystal had selective reflection (blue-green), indicating that its cholesteric pitch should be comparable to the wavelength of visible light.

48. Zugenmaier, P.; Steinmeier, H. *Polymer* **1986**, 27, 1601-1608.

49. Takahashi, Y.; Nishikawa, S. *Macromolecules* **2003**, 36, 8656-8661.

50. Norisuye, T. *Prog. Polym. Sci.* **1993**, 18, 543-584.

51. Teramoto, A.; Fujita, H. *Adv. Polym. Sci.* **1975**, 18, 65-149.

52. Teramoto, A. *Prog. Polym. Sci.* **2001**, 26, 667-720.

53. Chisaka, S.; Norisuye, T. *J. Polym. Sci., Part B: Polym. Phys.* **2001**, 39, 2071-2080.

54. Mansfield, M. L. *Macromolecules* **1986**, 19, 854-859.

**Table 1. Molecular Characteristics of ATBC Samples and Physical Properties in THF and MeOH at 25 °C**

Sample	DS <sup>d</sup>	PDI	in MeOH				in THF			
			$M_w/10^4$	$A_2^c$	$\langle S^2 \rangle_z^{1/2 f}$	$[\eta]^g$	$M_w/10^4$	$A_2^c$	$\langle S^2 \rangle_z^{1/2 f}$	$[\eta]^g$
ATBC1700K	3.0		167 <sup>a</sup>	0.7 <sup>a</sup>	53 <sup>a</sup>	209				1100
ATBC900K	3.0	1.15 <sup>h</sup>	87.0 <sup>a</sup>	1.1 <sup>a</sup>	38.5 <sup>a</sup>	131	90.0 <sup>a</sup>	3.2 <sup>a</sup>	70 <sup>a</sup>	617
ATBC700K	3.0	1.09 <sup>h</sup>	67.2 <sup>a</sup>	2.3 <sup>a</sup>	31 <sup>a</sup>	113	73.0 <sup>a</sup>	2.6 <sup>a</sup>	64 <sup>a</sup>	442
ATBC490K	3.0	1.03 <sup>h</sup>					49.0 <sup>a</sup>	2.8 <sup>a</sup>	47 <sup>a</sup>	382
ATBC460K	3.0	1.09 <sup>h</sup>	45.0 <sup>a</sup>	1.4 <sup>a</sup>	25.5 <sup>a</sup>	100	47.0 <sup>a</sup>	2.4 <sup>a</sup>	48.5 <sup>a</sup>	370
ATBC260K	3.2	1.06 <sup>h</sup>					26.3 <sup>a</sup>	3.3 <sup>a</sup>	33.0 <sup>a</sup>	
ATBC250K	2.8	1.07 <sup>h</sup>	24.0 <sup>a</sup>	1.8 <sup>a</sup>	18.5 <sup>a</sup>	58.7	25.5 <sup>a</sup>	2.7 <sup>a</sup>	32.0 <sup>a</sup>	180
ATBC130K	3.2	1.02 <sup>i</sup>	13.3 <sup>c</sup>	1 <sup>c</sup>		43.8				100
ATBC110K	3.2	1.05 <sup>i</sup>	10.5 <sup>c</sup>	1 <sup>c</sup>		34.0				70.8
ATBC55K	3.0	1.06 <sup>i</sup>	5.45 <sup>c</sup>	1 <sup>c</sup>	6.6 <sup>b</sup>	20.0				31.7
ATBC53K	3.2		5.30 <sup>a</sup>	4 <sup>a</sup>		21.0			7.7 <sup>b</sup>	
ATBC17K	3.4	1.04 <sup>i</sup>	1.66 <sup>c</sup>	4 <sup>c</sup>	2.85 <sup>b</sup>	7.1			2.75 <sup>b</sup>	8.4

<sup>a</sup> SLS. <sup>b</sup> SAXS. <sup>c</sup> Sedimentation equilibrium. <sup>d</sup> Elemental analysis. <sup>e</sup> In units of 10<sup>-4</sup>cm<sup>3</sup>mol g<sup>-2</sup>. <sup>f</sup> In units of nm. <sup>g</sup> In units of cm<sup>3</sup>g<sup>-1</sup>. <sup>h</sup>  $M_w/M_n$  (SEC-LS). <sup>i</sup>  $M_z/M_w$  (Sedimentation equilibrium)

**Table 2. Wormlike Chain Parameters for ATBC in THF, MeOH, and Their Mixtures at 25 °C**

Method	$M_L$ (nm <sup>-1</sup> )	$\lambda^{-1}$ (nm)	$d$ (nm)	$B$ (nm)
in THF				
$\langle S^2 \rangle_z$	$1750 \pm 50$	$78 \pm 4$	—	—
$P(k)$	$1780 \pm 30$	$78^a$	$1.1 \pm 0.1$	—
$[\eta]$	$1730 \pm 80$	$70 \pm 10$	$2.7 \pm 0.4$	—
in MeOH				
$\langle S^2 \rangle_z$	$1430 \pm 100$	$12 \pm 3$	—	$0.5 \pm 0.5$
$P(k)$	$1450 \pm 30$	$9 \pm 2$	$1.1 \pm 0.1$	—
$[\eta]$	$1440^a$	$11 \pm 1$	$2.2 \pm 0.1$	$0.2 \pm 0.2$
in the THF- MeOH mixture of $\phi_m = 0.5$				
$\langle S^2 \rangle_z$	$1700 \pm 50$	$35 \pm 3$	—	—
$P(k)$	$1730 \pm 30$	$35^a$	$1.3 \pm 0.2$	—
$[\eta]$	$1650 \pm 70$	$35 \pm 7$	$2.5 \pm 0.3$	—
in the THF- MeOH mixture of $\phi_m = 0.25$				
$P(k)$	$1750 \pm 30$	$45^a$	$1.2 \pm 0.1$	—
$[\eta]$	$1750^a$	$45 \pm 3$	$3.3 \pm 0.5$	—
in the THF- MeOH mixture of $\phi_m = 0.75$				
$P(k)$	$1530 \pm 30$	$16 \pm 3$	$1.3 \pm 0.1$	—
$[\eta]$	$1530^a$	$17 \pm 1$	$2.7 \pm 0.5$	—

<sup>a</sup> Assumed

**Table 3.** Values of  $h$  and  $\lambda^{-1}$  for ATBC in THF-MeOH mixtures at 25 °C

$\phi_m$	$h$ (nm)	$\lambda^{-1}$ (nm)
0 (THF)	$0.26 \pm 0.01$	$75 \pm 5$
0.25	$0.26 \pm 0.01$	$45 \pm 3$
0.5	$0.27 \pm 0.01$	$35 \pm 3$
0.75	$0.30 \pm 0.01$	$17 \pm 2$
1 (MeOH)	$0.32 \pm 0.01$	$11 \pm 2$

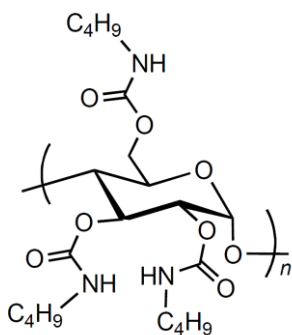


**Chart 1.** Chemical structure of ATBC.

## Figure captions

**Figure 1.** Plots of  $M_{\text{app}}^{-1/2}$  vs  $\bar{c}$  in MeOH at 25 °C (a) and those of  $(Kc/R_0)^{1/2}$  vs  $c$  in MeOH (b) and THF (c) at 25 °C.

**Figure 2.** Berry plots for indicated ATBC samples in THF (filled circles) and in MeOH (open circles) at 25 °C. (a) SLS in MeOH. (b) SLS in THF. (c) (d) SAXS.

**Figure 3.** Molecular weight dependence of  $\langle S^2 \rangle_z^{1/2}$  for ATBC in THF (filled circles), MeOH (open circles), and a THF-MeOH mixture of  $\phi_m = 0.5$  (triangles) at 25 °C. Solid curves, theoretical values calculated for the wormlike chains with the parameters in Table 2. The dashed curve shows the theoretical values for  $B = 0$ .

**Figure 4.** Molecular weight dependence of  $[\eta]$  for ATBC in THF (filled circles), MeOH (open circles), and their mixtures (inverted triangles,  $\phi_m = 0.25$ ; triangles,  $\phi_m = 0.5$ ; squares,  $\phi_m = 0.75$ ) at 25 °C. Solid curves, theoretical values calculated for the wormlike chains with the parameters in Table 2. The dashed curve shows the theoretical values for  $B = 0$ .

**Figure 5.** Holtzer plots for ATBC samples in THF, MeOH, and their mixtures at 25 °C. Solid curves, theoretical values for the unperturbed wormlike cylinders with the parameters in Table 2. Dashed curves, theoretical values in the rod limit ( $\lambda^{-1} = \infty$ ).

**Figure 6.** IR spectra (molar absorption coefficient  $\varepsilon$  vs wavenumber) for ATBC460K in mixtures of THF and MeOH with indicated  $\phi_m$  at room temperature (20 – 25 °C).

**Figure 7.**  $\phi_m$ -dependence of  $-\langle \alpha \rangle_{280}$  (filled symbols) and  $f_{1698}$  (open symbols) for ATBC900K (circles), ATBC460K (triangles), ATBC55K (squares), and ATBC17K (inverted triangles).

**Figure 8.** Plots of (a)  $h^{-1}$  vs  $\lambda$  and (b)  $h$  and  $\lambda h$  vs  $f_{1698}$  for ATBC in mixtures of THF and MeOH.

**Figure 9.** A possible 3D structure of rigid helical ATBC (6-fold helix and  $h = 0.25$  nm). (a) Side view. (b) Top view.

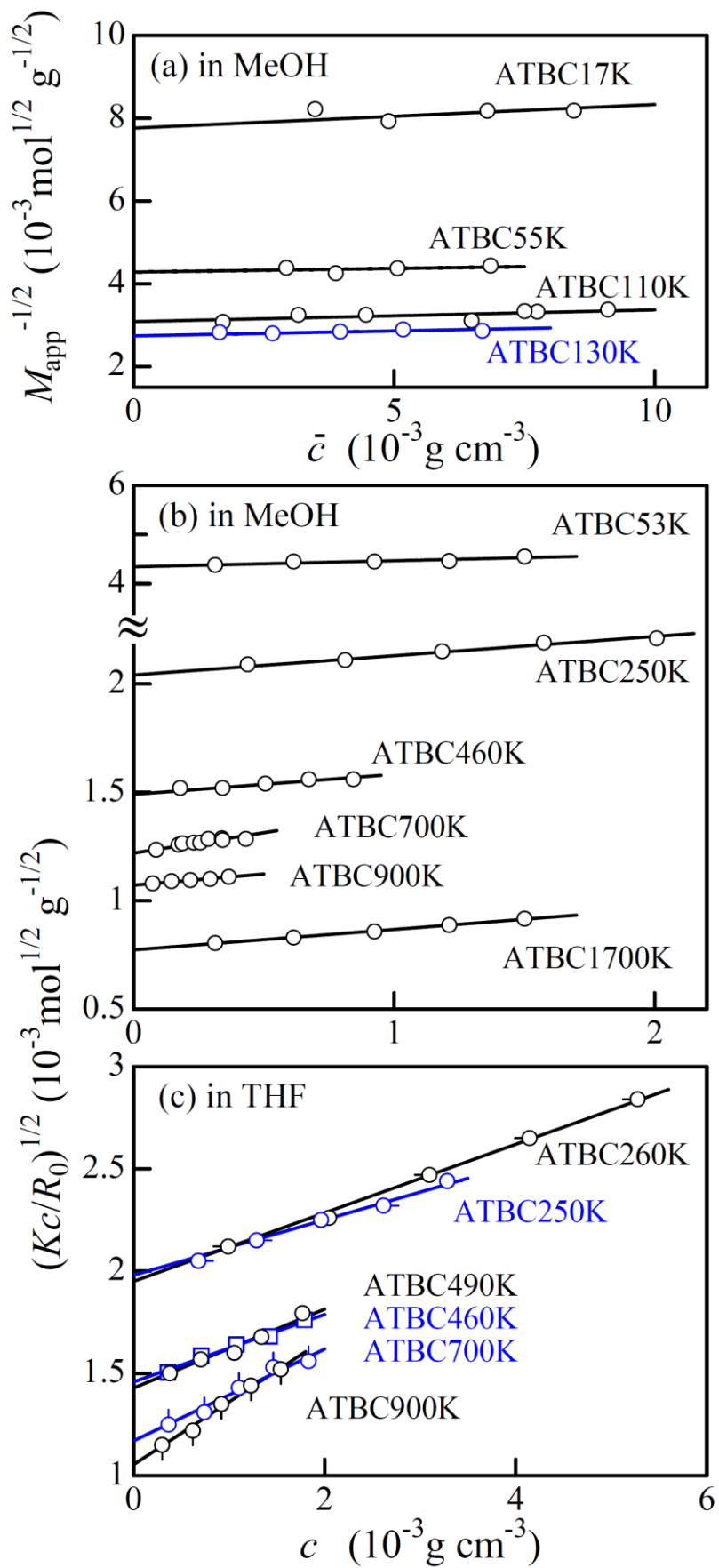


Figure 1. Terao et al.

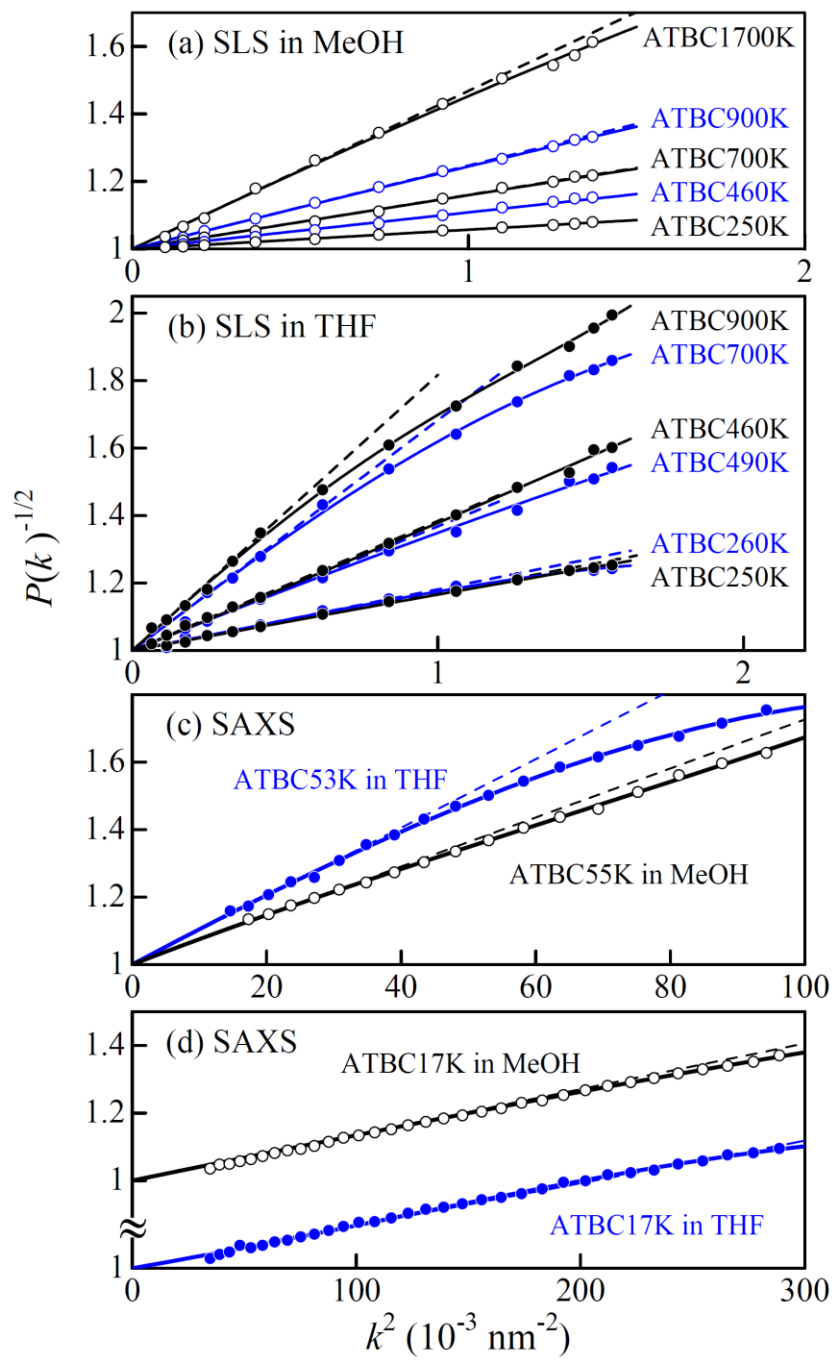


Figure 2. Terao et al.

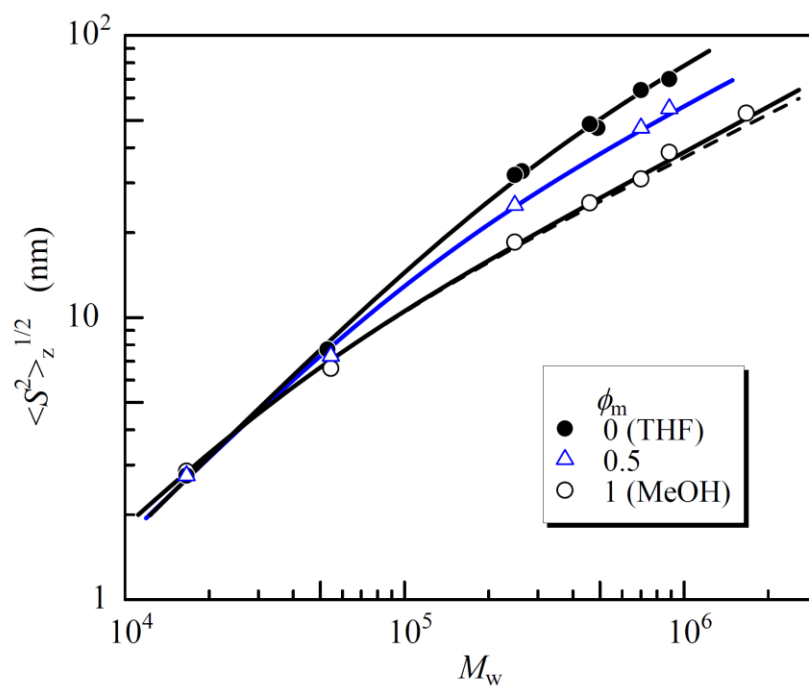


Figure 3. Terao et al.

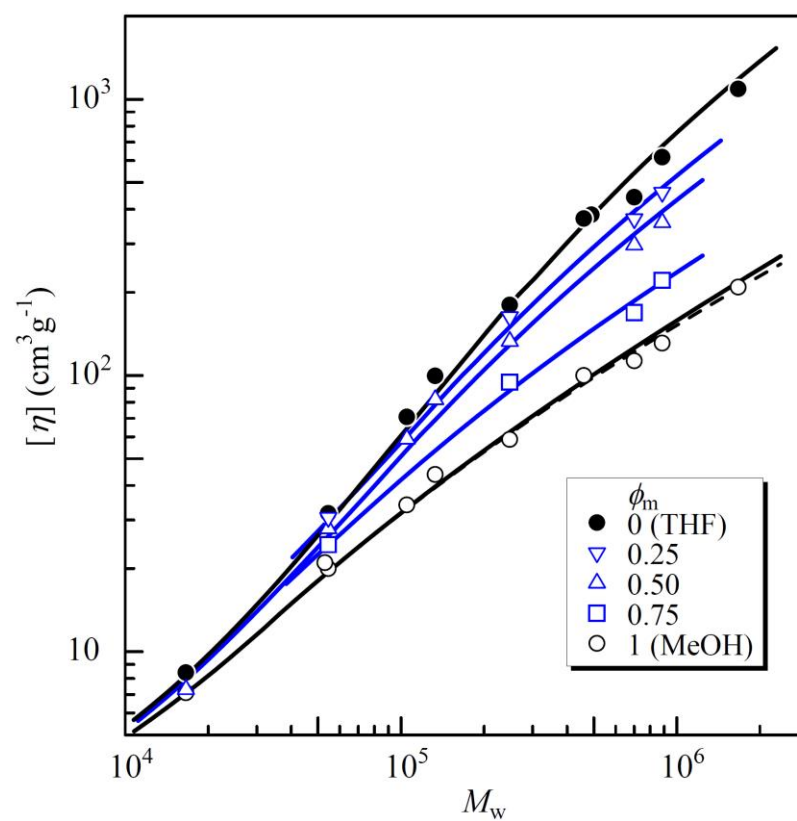
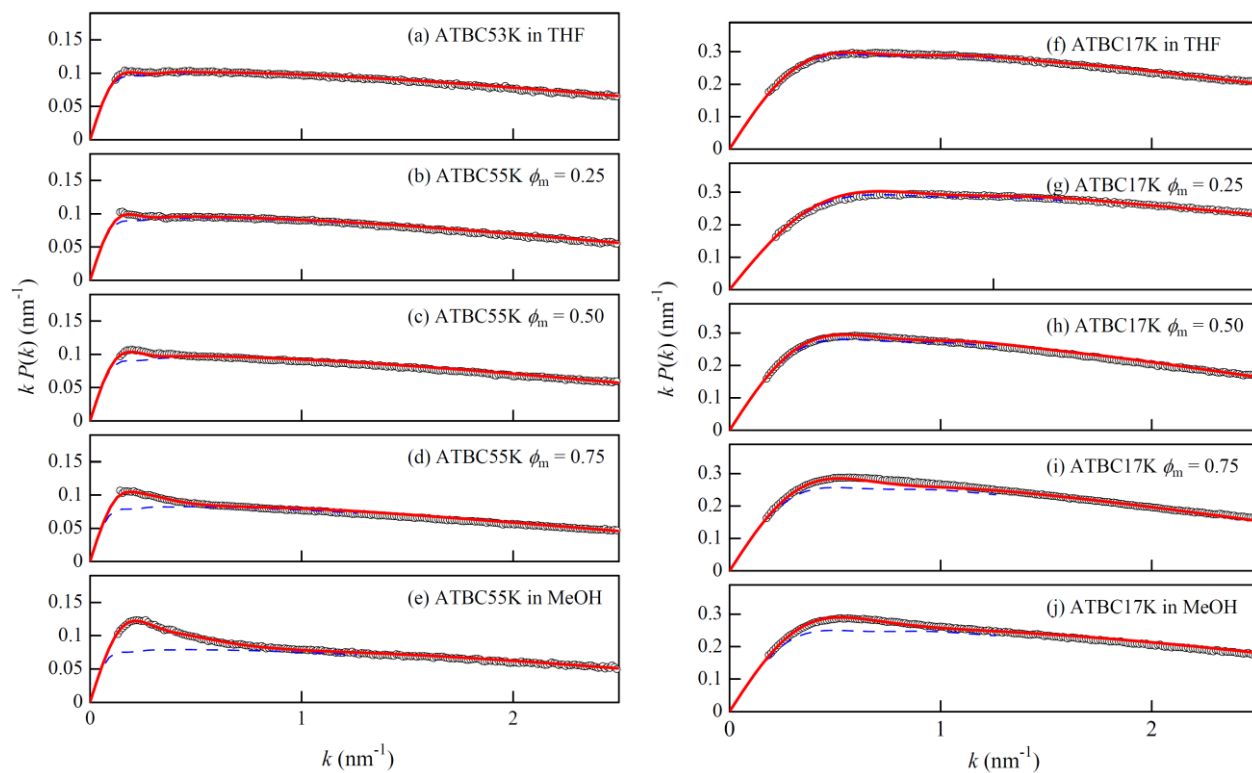
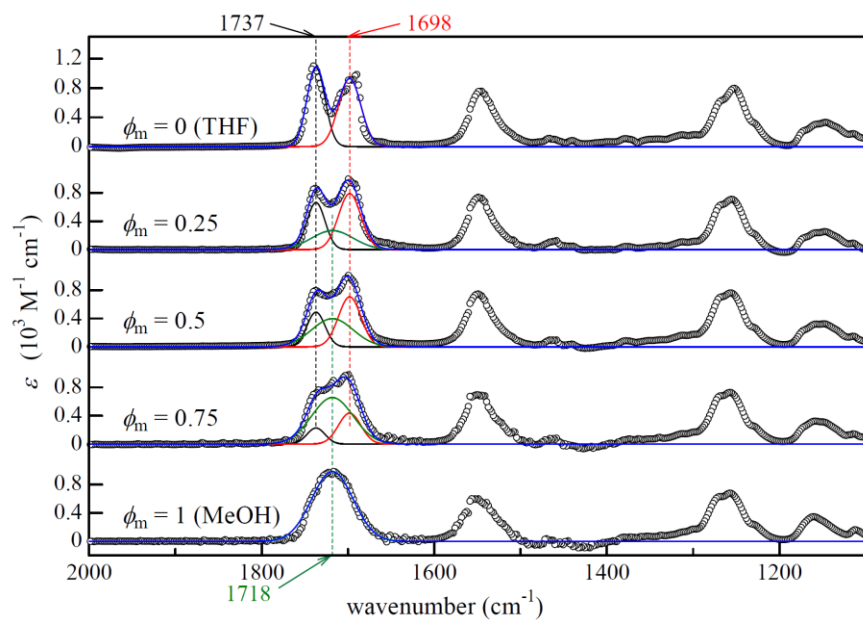


Figure 4. Terao et al.



**Figure 5. Terao et al.**



**Figure 6. Terao et al.**

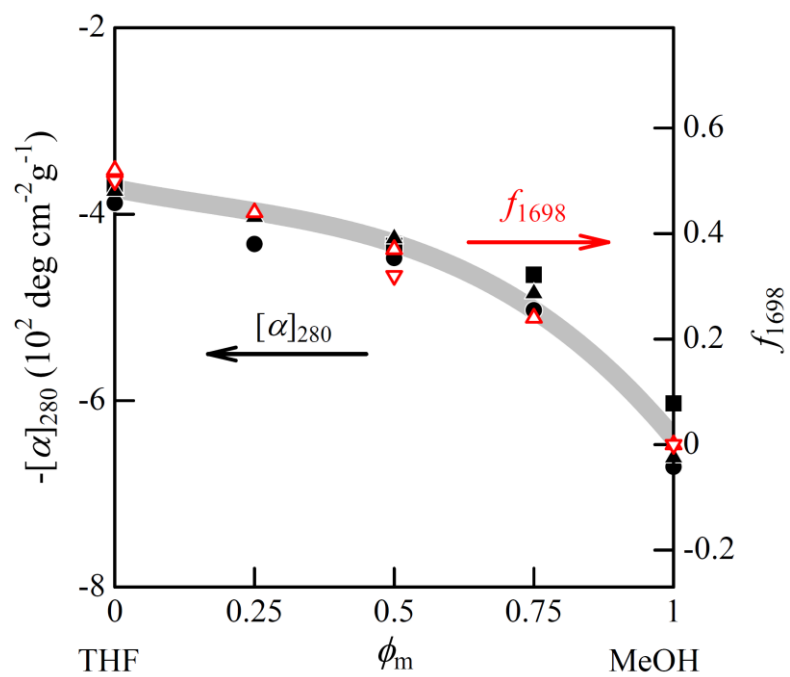


Figure 7. Terao et al.

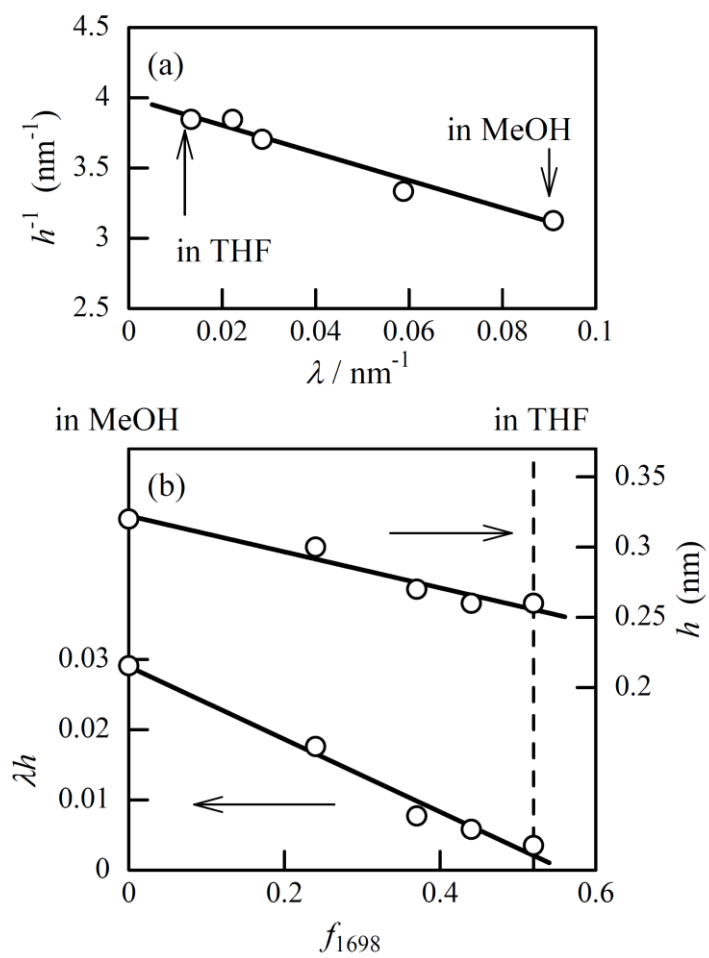
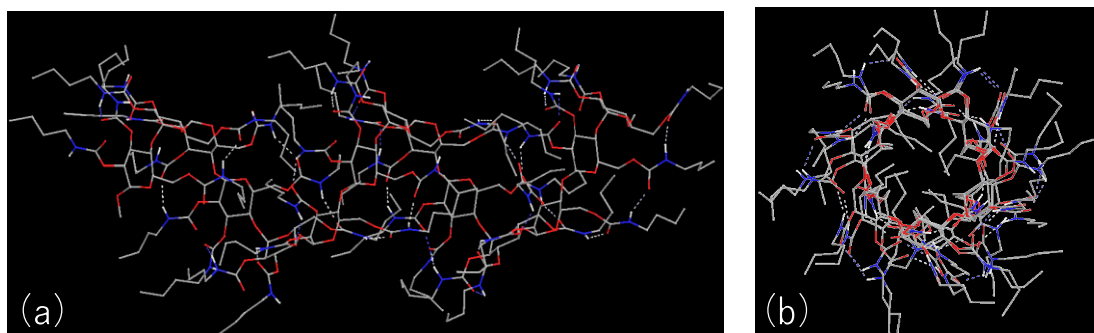


Figure 8. Terao et al.



**Figure 9. Terao et al.**

## Table of Contents

